



OPEN

A nontraditional method for reducing thermoelastic stresses of variable thickness rotating discs

A. M. Eldeeb¹, Y. M. Shabana^{1,2}, T. A. El-Sayed^{1✉} & A. Elsayaf³

Stresses reductions and/or raising the load-carrying capacity for a mechanical structure are always great dilemmas for researchers. In this article, a novel method is proposed, and its efficiency is examined for achieving these goals on functionally graded rotating nonuniform thickness discs. The originality of this method relies on comprising a geometrically well-defined area, into the whole structure, with certain homogeneous properties including density, thermal expansion coefficient, and elasticity matrix. This area acts as a reducer of the maximum values of various stress components. The solution of the magnetoelastic/magneto-thermoelastic problem is accomplished using the finite element method. The disc is subjected to partial uniform outer pressure, whereas, upon applying thermal loads; the thermal boundary conditions are considered symmetric. The proposed method is found to be beneficial as the obtained results demonstrated the ability to reduce the maximum stresses with different percentages depending on the location, angular width, and properties of the predefined area. This is reflected by an attainable decrease in the maximum compressive tangential stress and the von Mises stress by approximately 20.7% and 12.5%, respectively, under certain conditions.

Functionally graded materials (FGMs) have gained significant attention in the engineering community for their exceptional properties compared to traditional laminated composites and are widely used in severe working conditions^{1,2}. Rotating discs, which are crucial components in many engineering systems, are often made of FGMs. Numerous studies have explored their elastic^{3,4}, thermoelastic^{5,6}, and elastoplastic static behaviors⁷⁻⁹. The dynamic performance of rotating discs has also been investigated in several studies¹⁰⁻¹². Additionally, the effects of asymmetric loading conditions on their performance has been examined in some research^{13,14}.

On the other hand, other scholars considered the magnetoelastic (ME) and magneto-thermoelastic (MTE) behaviors of discs (and their counterparts: cylinders and spheres), which are core items of many applications, such as aerospace industry, supersonic airplanes, rockets/missiles, submarine structures, nuclear energy, electronics, biomedical sector, geophysics, turbines/pumps/compressors rotors, optics, pipes, brake discs, internal combustion engines, ME sensors and actuators¹⁵⁻¹⁸. For example, Rad and Shariyat¹⁹ developed a 3D model for FGM discs prone to nonuniform loadings. Additionally, different solution techniques were proposed to obtain the MTE performance of symmetric structures (disc/cylinder/sphere)^{20,21}. These methods include for instance the finite element method (FEM) that was used by Zenkour and Abbas¹⁶ to study the effects of the FGM's heterogeneity index on the disc's stresses. Moreover, Zenkour²² and Dini et al.¹⁸ obtained the steady MTE behaviors of multi-layer discs.

In the same vein, different means are sought to alleviate the stresses and/or enhance the sustainability (e.g., loading limits and failure likelihood) of any structure. For example, performing optimization for some parameters is found to be advantageous²³⁻²⁵. Also, the concept of grading the material properties along two simultaneous directions has its positive gain²⁶⁻²⁸. In addition, controlling a material's microstructure, to have a new substance with certain aspired properties²⁹ (e.g., yield strength³⁰), is also beneficial. The latter seems to be complicated; however, with the grand advancement in technology and fabrication techniques, it became attainable and easily accomplished. For instance, two methods are being used for this sake: modified slip-casting method³¹ and fused deposition modeling method³².

¹Mechanical Design Department, Faculty of Engineering, Helwan University, P.O. Box 11718, El-Matara, Cairo, Egypt. ²Department of Astronautic Science and Mechanics, Harbin Institute of Technology, Harbin 150001, PR China. ³Mechanical Engineering Department, College of Engineering and Technology-Cairo Campus, Arab Academy for Science, Technology and Maritime Transport (AASTMT), Cairo, Egypt. ✉email: Tamer_alsayed@m-eng.helwan.edu.eg

In light of the extensive literature, efforts are being exerted on exploring methods to mitigate the stress and increase the loading capacity of rotating discs. Thus, this article proposes a novel and atypical approach to material customization under asymmetric loading conditions. This unconventional method involves incorporating a predefined area within the disc's FGM domain that has constant values for selected properties. The primary objective of this novel area is to reduce induced stress levels. The article explores through the FEM the effects of this area, including its properties, angular width, and position, on the disc's MT and MTE behaviors. The judgment on the success or failure of the proposed idea will be evaluated based on the reduction of the maximum stress components including the von Mises stress, to avoid plasticity occurrence.

Problem formulation

In polar coordinates ($r\theta z$), Fig. 1 depicts a disc with inner and outer radii r_i and r_o , respectively. The disc has a nonuniform thickness $h = h(r)$, and rotates with angular speed ω . It is comprised of two portions with distinct properties. One portion is formed of FGM (i.e., $\psi > \theta > \psi + \phi$), while the other, named as the prescribed area ($\psi \leq \theta \leq \psi + \phi$), is made of a material with selected constant properties. The angles ψ and ϕ will be defined in the following section, and θ_p is the angle of the applied outer pressure.

The thermomechanical equilibrium equations are written as³³:

$$\frac{1}{rh} (rhk_r T_{,r})_{,r} + \frac{1}{r^2 h} (hk_\theta T_{,\theta})_{,\theta} = 0 \tag{1}$$

$$(rh\sigma_{rr})_{,r} + (h\sigma_{r\theta})_{,\theta} - h\sigma_{\theta\theta} + F_r + rhf_r = 0 \tag{2}$$

$$(rh\sigma_{r\theta})_{,r} + (h\sigma_{\theta\theta})_{,\theta} + h\sigma_{r\theta} + F_\theta + rhf_\theta = 0 \tag{3}$$

where the comma denotes partial differentiation, T is the temperature, and $\mathbf{k} = \begin{bmatrix} k_r & 0 \\ 0 & k_\theta \end{bmatrix}$ is the thermal conductivity. $F_r = \rho h \omega^2 r^2$ is the centrifugal force, and $F_\theta = \rho h \omega_t r^2$ is the tangential force that exists when $\omega_t \neq 0$, where t is the time variable, and ρ represents the material's density. In terms of h , it is proposed to change with the radial position r through the following relation³⁴:

$$h(r) = H \left(1 - \alpha_1 \left(\frac{r}{r_o} \right) \right)^{\alpha_2} \tag{4}$$

with H is an imaginary thickness at $r = 0$, and α_j ($j = 1, 2$) is a geometrical parameter.

Furthermore, since the disc has a large diameter-to-thickness ratio; the state of plane stress becomes a valid hypothesis; hence, the constitutive relation is³⁵:

$$\boldsymbol{\sigma} = \mathbf{C}\boldsymbol{\varepsilon} - \lambda T \tag{5}$$

where $\boldsymbol{\sigma}$ is the stress field of three components: σ_{rr} , $\sigma_{\theta\theta}$, and $\sigma_{r\theta}$ that are the radial, tangential, and shear stresses, respectively. Also, \mathbf{C} is the elasticity matrix with the following non-zero components: $C_{11} = \frac{E}{1-\nu^2}$, $C_{12} = \frac{E\nu}{1-\nu^2}$ and $C_{66} = \frac{C_{11}-C_{12}}{2}$, where E and ν resemble the material's elastic modulus and Poisson's ratio, respectively. Besides, $\boldsymbol{\varepsilon}$ refers to the strain components given through the kinematics relation (Eq. (6)), with u and ϑ are the radial and

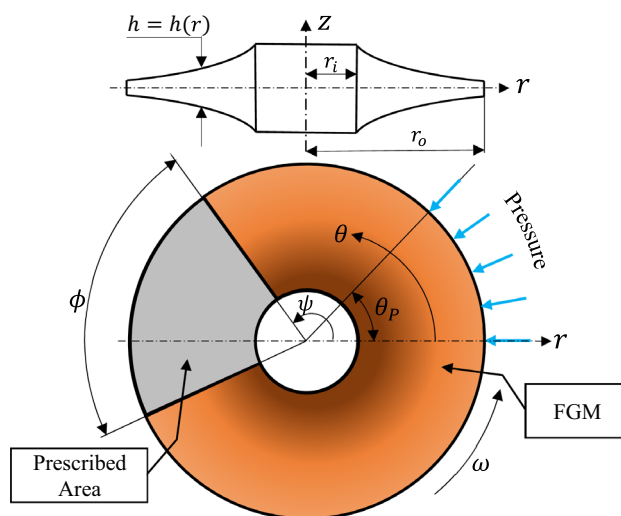


Figure 1. Schematic drawing of the proposed rotating annular variable thickness disc. The gradient-filled brown area represents the FGM, while the gray area, with an angular width of ϕ , is made of homogeneous material with constant selected properties. The outer pressure angle is denoted by θ_p .

tangential displacements, in turns³⁴. In addition, λ (stress-temperature coefficient vector) is calculated through Eq. (7) with α is the thermal expansion coefficient vector³⁶.

$$\boldsymbol{\varepsilon} = \begin{Bmatrix} \varepsilon_{rr} \\ \varepsilon_{\theta\theta} \\ 2\varepsilon_{r\theta} \end{Bmatrix} = \begin{Bmatrix} u_{,r} \\ (u + \vartheta_{,\theta})/r \\ \vartheta_{,r} + (u_{,\theta} - \vartheta)/r \end{Bmatrix} \tag{6}$$

$$\boldsymbol{\lambda} = \mathbf{C}\boldsymbol{\alpha} \rightarrow \begin{Bmatrix} \lambda_1 \\ \lambda_2 \\ \lambda_3 \\ \lambda_6 \end{Bmatrix} = \begin{bmatrix} C_{11} & C_{12} & C_{12} & 0 \\ & C_{11} & C_{12} & 0 \\ & & C_{11} & 0 \\ sym & & & C_{66} \end{bmatrix} \begin{Bmatrix} \alpha_1 \\ \alpha_2 \\ \alpha_3 \\ 0 \end{Bmatrix} \tag{7}$$

Moreover, in Eqs. (2) and (3), the two components of f_j ($j = r, \theta$) are related to Lorentz force arising due to the presence of the constant and axial magnetic field (\mathcal{H}_z), and are given as³⁷:

$$f_r = \mu \mathcal{H}_z^2 (u_{,r} + \frac{u}{r} + \frac{1}{r} \vartheta_{,\theta})_{,r}, f_{\theta} = \frac{\mu \mathcal{H}_z^2}{r} (u_{,r} + \frac{u}{r} + \frac{1}{r} \vartheta_{,\theta})_{,\theta} \tag{8}$$

where $\mu = \mu_0 \eta$ is the material's magnetic permeability with $\mu_0 = 4\pi \times 10^{-7}$ H/m is the permeability of space, and η is the material's relative magnetic permeability¹⁸.

Material gradation

In the current analyses, the disc is made of two parts with dissimilar material compositions. The first part is made of FGMs (the gradient-filled brown area shown in Fig. 1). The material properties are radially graded as follows³⁸:

$$\beta(r, \psi > \theta > \psi + \phi) = \beta_m + (\beta_c - \beta_m) \left(\frac{r - r_i}{r_o - r_i} \right)^j \tag{9}$$

where β denotes a generic material property, and j refers to the heterogeneity index. Also, the two subscripts m and c stand for metal and ceramic, respectively.

Conversely, the other part, or area, of the disc, which has an angular width of ϕ and named as the prescribed area (shaded in gray in Fig. 1), is located at angle ψ . This area is assumed to be perfectly bonded to the FGM area. It is introduced to be examined as being effective as an unconventional method in reducing the disc's induced stresses. In addition, it has special material characteristics compared to the FGM area. It has specific and constant selected properties (β^*). The rest of the properties, other than the selected ones, would follow Eq. (9). In other words, this area has:

$$\beta^*(r, \psi \leq \theta \leq \psi + \phi) = x\beta^* \beta_{\xi\beta^*} \quad (\xi_{\beta^*} = m \text{ or } c) \tag{10}$$

where x is named as the property fraction, which is a positive number (0.25, 0.5 or 1), and ξ_{β^*} is a symbol standing for either m or c . For simplicity, β^* would include either of ρ , α and \mathbf{C} . In practical applications, this idea can be achieved through controlling the microstructure of the materials that can be conducted by the material's processing approach with the aid of the great advancement and technology available globally.

Finite element formulation

A finite element (FE) algorithm is built by the authors through the MATLAB software to solve for $\mathbf{X} = \{ \mathbf{U} \ \mathbf{T} \}$, where $\mathbf{U} = \{ u \ \vartheta \}$. In FEM, \mathbf{X} is connected to its nodal values through the shape functions (N)^{39,40}:

$$\mathbf{X} \approx \sum_{i=1}^{n_n} N_i^e \mathbf{X}_i \tag{11}$$

where n_n is the number of nodes per element, and N_i^e is read as: N at the i th node of the element e .

Thereafter, the FE symbolic equation ($\mathbf{K}\mathbf{X} = \mathbf{R}$) is derived using the standard Galerkin's procedures³⁹. In that equation, \mathbf{K} represents the global stiffness matrix, and \mathbf{R} denotes the external force vector. That symbolic equation is expanded as below³⁹:

$$\sum_{e=1}^{n_e} \left(\begin{bmatrix} \mathbf{K}_{UU}^e & \mathbf{K}_{UT}^e \\ 0 & \mathbf{K}_{TT}^e \end{bmatrix} \begin{Bmatrix} \mathbf{U}^e \\ \mathbf{T}^e \end{Bmatrix} = \begin{Bmatrix} \mathbf{R}_U^e \\ 0 \end{Bmatrix} \right) \tag{12}$$

with n_e is the total number of elements. Each term in Eq. (12) is calculated as follows:

$$\begin{cases} \mathbf{K}_{UU}^e = \int_{\Omega_e} rh [\mathbf{B}_U] [\mathbf{C}] [\mathbf{B}_U] d\Omega_e - \int_{\Omega_e} rh \mu \mathcal{H}_z^2 [\hat{\mathbf{N}}] [\mathbf{B}_\mu] [\mathbf{f}] d\Omega_e \\ \mathbf{K}_{UT}^e = - \int_{\Omega_e} rh [\mathbf{B}_U] [\boldsymbol{\lambda}] [\mathbf{N}] d\Omega_e \\ \mathbf{K}_{TT}^e = \int_{\Omega_e} rh [\mathbf{B}_T] [\mathbf{k}] [\mathbf{B}_T] d\Omega_e \\ \mathbf{R}_U^e = \int_{\Gamma} rh [\mathbf{N}] \sigma_n d\Gamma + \int_{\Omega_e} [\mathbf{N}] [\mathbf{F}] d\Omega_e \end{cases} \tag{13}$$

where $[\hat{\mathbf{N}}] = \begin{bmatrix} [\mathbf{N}] & [\mathbf{N}] \\ [\mathbf{N}] & [\mathbf{N}] \end{bmatrix}_{2n_n \times 2}$, $\mathbf{F} = \begin{Bmatrix} F_r \\ F_\theta \end{Bmatrix}$, and $\mathbf{f} = \begin{Bmatrix} f_r \\ f_\theta \end{Bmatrix}$.

Mechanical property [†]		Boundary conditions	
Elastic modulus (GPa)	Poisson's ratio		
$E_i = 200$	$\nu_i = 0.28$	$\sigma_{rr}(r_i, \theta) = P_0 \cos(2\theta)$	$\sigma_{rr}(r_o, \theta) = 0$
$E_o = E_i/3$	$\nu_o = 0.28$	$\sigma_{r\theta}(r_i, \theta) = 0$	$\sigma_{r\theta}(r_o, \theta) = 0$

Table 1. Mechanical properties and boundary conditions of FGM cylinder³⁸. † Eq. (9) is used to describe the variation of E and ν with $j = 1$.

The integrations of Eq. (13) are accomplished through the gauss quadrature method with nine gauss points within each element that has an area of Ω_e , such that $d\Omega_e = drd\theta$. In addition, σ_n identifies the traction on a certain part Γ of the boundary^{39,41}. Furthermore, \mathbf{B}_U represents the strain–displacement matrix, \mathbf{B}_T is the gradient matrix (see for instance Refs^{39,42} for their definitions.), and \mathbf{B}_μ is related to the magnetic field and is determined as follows:

$$\mathbf{B}_\mu = \begin{bmatrix} [\mathbf{N}]_{,rr} + [\mathbf{N}]_{,r}r^{-1} - [\mathbf{N}]r^{-2} & [\mathbf{N}]_{,r\theta}r^{-1} - [\mathbf{N}]_{,\theta}r^{-2} \\ [\mathbf{N}]_{,r\theta}r^{-1} + [\mathbf{N}]_{,\theta}r^{-2} & [\mathbf{N}]_{,\theta\theta}r^{-2} \end{bmatrix}_{2 \times 2n_n} \quad (14)$$

Finally, \mathbf{X} can be easily obtained using matrix calculus. Then, ϵ and σ are computed directly after applying the proper boundary conditions⁴¹.

Algorithm verification

In this section, the validity of the proposed FEM formulation is examined through regenerating the results of three examples that exist in previous literature.

The first example is a nonuniform thickness clamped-free disc studied using the Runge–Kutta’s method by Hassani et al.⁴³. It rotates with $\omega = 300\text{rad/s}$, and is prone to a temperature field defined by Eq. (15). Geometrically, the disc’s thickness is defined via the power-law given in Eq. (16) with $r_i = 0.1\text{m}$ and $r_o = 0.6\text{m}$. Table 1 in Ref⁴³ lists the numerical values of the material properties that were graded according to Eq. (9) with $j = 2$. Since this problem is completely symmetric ($\sigma_{r\theta} = 0$); there is no need to investigate the 360° model of the disc. Only its quarter is modeled with proper symmetric boundary conditions (BCs) at $\theta = 0^\circ$ and 90° ⁴¹. Figure 2 shows the distribution of stresses obtained by the current FEM solution and the method used by Hassani et al.⁴³.

$$T(r) = 100 + (300 - 100) \left(\frac{r - r_i}{r_o - r_i} \right)^2 \text{ (}^\circ\text{C)} \quad (15)$$

$$h(r) = 0.1(r/r_o)^{0.5} \text{ (m)} \quad (16)$$

The second example is presented to verify the solution ability in obtaining the ME behaviors of a nonrotating cylinder with $r_i = 0.2r_o$. It was subjected to uniform magnetic field ($\mathcal{H}_z = 2.23 \times 10^9\text{A/m}$), with the magnetic permeability varying as $\mu = \mu_0 \times r^{-221}$. The outer surface was free-of-stress, while at $r = r_i$ a uniform and

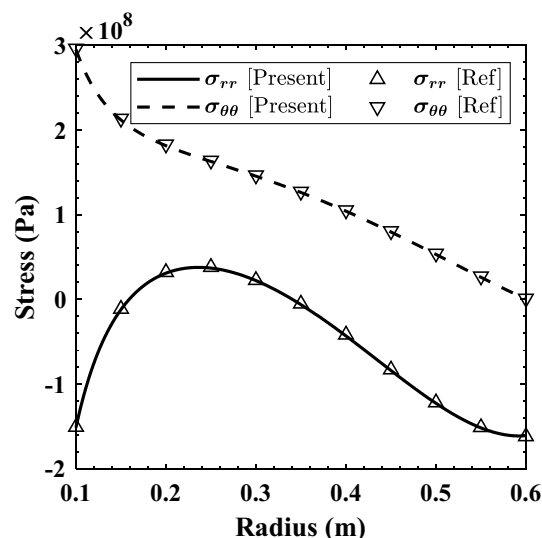


Figure 2. Comparison between the stresses’ distributions obtained through FEM and in Ref⁴³ at $\theta = 0^\circ$.

symmetric pressure with a value of P_0 existed; thus, symmetric BCs prevails. Also, the following quantities were used: $\frac{E(1-\nu)}{(1+\nu)(1-2\nu)} = 47.3\text{GPa}$, and $\frac{E\nu}{(1+\nu)(1-2\nu)} = 28.8\text{GPa}^{21}$; so that, after some mathematical manipulations, it yields:

$$E = 25.5 \times r^{-2} \text{ GPa}, \nu = 0.378 \tag{17}$$

However, in this example the plane strain conditions were used; therefore, this conversion is conducted to Eq. (5)⁴⁴:

$$E = E/(1 - \nu^2), \nu = \nu/(1 - \nu) \tag{18}$$

Results are presented in a dimensionless form according to Eq. (19), which is used henceforth, and are depicted in Fig. 3.

$$\bar{\sigma}_{ij} = \sigma_{ij}/P_0, (i, j = r, \theta) \tag{19}$$

The third and final example is a nonrotating cylinder (plane strain) with $r_o = 3r_i$ studied by Li and Liu³⁸. Table 1 lists the numeric values of the mechanical properties, and the associated BCs with $P_0 = 100\text{MPa}$. This

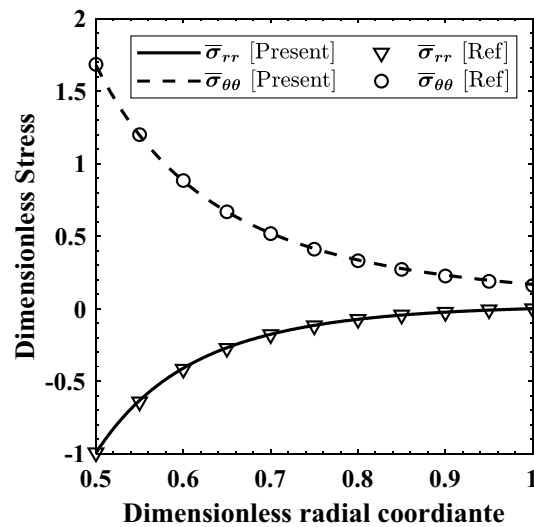


Figure 3. Dimensionless stresses distributions for a cylinder subjected to magnetic field.

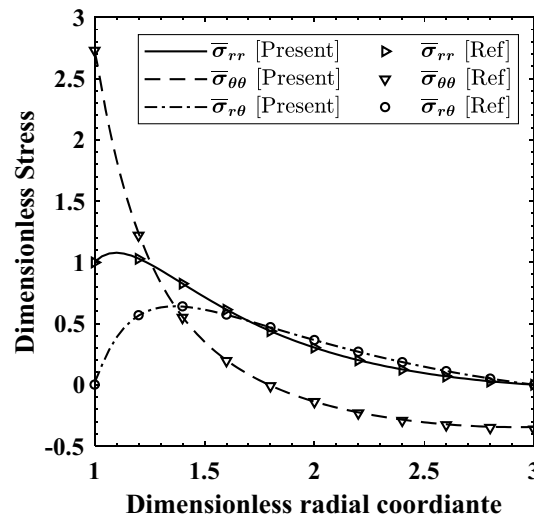


Figure 4. Comparison between the radial variation of $\bar{\sigma}_{rr}$, $\bar{\sigma}_{\theta\theta}$, and $\bar{\sigma}_{r\theta}$ calculated through the current FE algorithm and in Ref.³⁸. $\bar{\sigma}_{rr}$ and $\bar{\sigma}_{\theta\theta}$ are drawn at $\theta = 0^\circ$, and $\bar{\sigma}_{r\theta}$ is calculated at $\theta = 45^\circ$.

example is re-examined to benchmark the capability of solving models with asymmetric BCs. Figure 4 portrays the resulting dimensionless stresses.

It is observed from the previous three verification examples that the obtained outcomes using the present model are in coherence with the results published in the literature. Therefore, the current solution scheme is robust and can be used for predicting the behaviors of discs with different loads and various boundary conditions.

Results and discussion

As intended in this work, mitigation of the induced ME and MTE stresses of a nonuniform thickness FGM disc is sought. This is accomplished through fixing one property or more within the prescribed area of the disc's domain. On the other hand, the disc has inner and outer radii of 0.2m and 0.5m, respectively. The parameters of Eq. (4) are: $H = 0.1\text{m}$, $\nu_1 = 0.415196$, and $\nu_2 = 3^8$. It rotates with $\omega = 700\text{rad/s}$ ($\omega_t = 0$; thus $F_\theta = 0$), and is subjected to an axial magnetic field of $\mathcal{H}_z = 10^6\text{A/m}$.

Table 2 lists the material properties assigned in this work. Equation (9) labels the FGM gradation model ($j = 1$), and Eq. (10) describes the selected properties variation within the predefined area. Also, ϕ is set to 45° , and ψ has a value of 0° , 90° , or 180° .

Concerning the FE scheme, the eight-node ($n_n = 8$) isoparametric 2D element is used to discretize the disc's domain. It is found that convergence occurs at $n_e = 20000$ elements after examining different numbers of elements.

Case (1): Magnetoelastic (ME) loading. In the beginning, the analysis commences with a disc having a fixed inner surface ($u(r_i, \theta) = \vartheta(r_i, \theta) = 0$), and is subjected to partial uniform normal loading at the outer surface; such that $\sigma_{rr}(r_o, 0 \leq \theta \leq \theta_p) = -P_0$, where $P_0 = 100\text{MPa}$ and $\theta_p = 45^\circ$ (see Fig. 1 for its description). For the sake of comparison, Fig. 5 depicts the ME response using Eq. (9) only.

It is observed from Fig. 5a that $\bar{\sigma}_{rr_{max}}$ and $\bar{\sigma}_{rr_{min}}$ stood at ~ 1.5 and -1 , respectively. The critical tensile $\bar{\sigma}_{\theta\theta}$ is found to be almost 0.92 (Fig. 5b), while the maximum compressive value is negligible (henceforth *max* and *min* denote the greatest values of tensile and compressive stresses in turns). Also, due to the lack of shear traction on any surface; the upper and lower limits of $\bar{\sigma}_{r\theta}$ (Fig. 5c) have similar value of approximately ± 0.27 . Therefore, it can be concluded that the role of $\bar{\sigma}_{rr_{min}}$, $\bar{\sigma}_{\theta\theta_{min}}$ and $\bar{\sigma}_{r\theta}$ is negligible compared to $\bar{\sigma}_{rr_{max}}$ and $\bar{\sigma}_{\theta\theta_{max}}$.

In order to decrease the values of the extreme stresses, Eq. (10) is used along with Eq. (9) yielding an area with certain homogeneous material properties. Table 3 lists the ME stress values at different values of ψ , and x_{β^*} while β^* included ρ only.

It is seen that the variation of ψ and x_ρ led to an increase in the values of $\bar{\sigma}_{rr_{max}}$ due to change in F_r . For example, this growth reached 2.5% at $\psi = 0^\circ$, $x_\rho = 1$ and $\xi_\rho = c$. Alternatively, at $\psi = 90^\circ$, $x_\rho = 0.5$ and $\xi_\rho = c$, a marginal increase is detected ($< 0.2\%$). In terms of $\bar{\sigma}_{\theta\theta_{max}}$, a swing in behavior can be witnessed. At $x_\rho = 0.5$ or 1, and $\xi_\rho = m$, $\bar{\sigma}_{\theta\theta_{max}}$ dropped by around 5% at $\psi = 180^\circ$, while it increased to 1.074 at $\psi = 0^\circ$ with $x_\rho = 0.5$ and $\xi_\rho = m$. Also, using $\psi = 0^\circ$ would yield larger stresses compared to $\psi = 90^\circ$ and 180° under this state of loading. Additionally, it is noticed that using $x_\rho = 0.5$ with $\xi_\rho = c$ would yield nearly analogous results to the case of using $\xi_\rho = m$ at $x_\rho = 1$.

	E (GPa)	ρ (kg/m^3)	k^\dagger (W/mK)	η	ν	α^\ddagger ($10^{-6}/^\circ\text{C}$)
Metal (Aluminum)	70	2700	233	2.3	0.35	23.4
Ceramic (Zirconia)	151	5700	2.09	1	0.3	10

Table 2. Material properties of the FGM constituents^{16,18}. $^*k_r = k_\theta = k$. $^\dagger\alpha_1 = \alpha_2 = \alpha_3 = \alpha$.

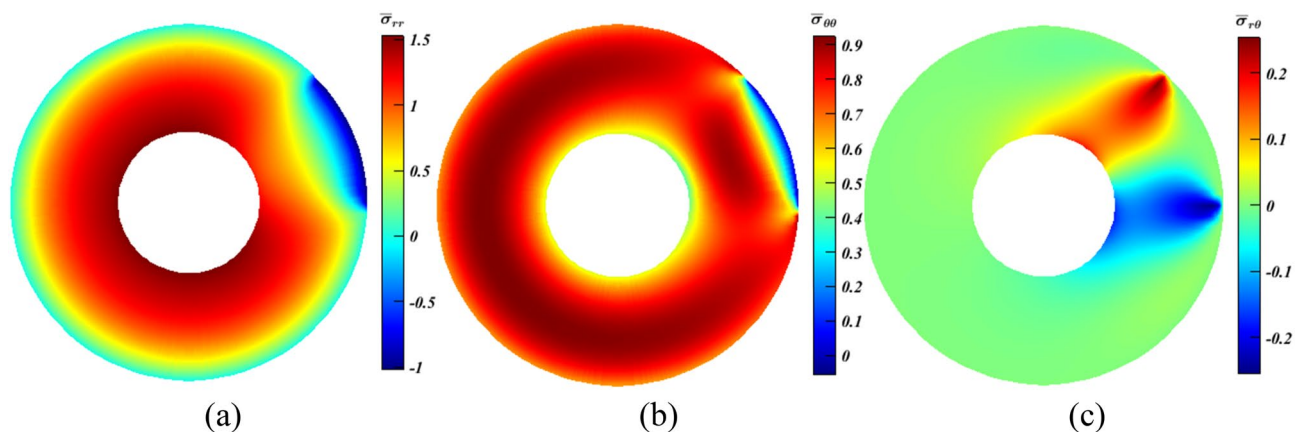


Figure 5. Dimensionless stress contours for a rotating disc under partial normal pressure. (a) $\bar{\sigma}_{rr}$, (b) $\bar{\sigma}_{\theta\theta}$, and (c) $\bar{\sigma}_{r\theta}$.

Stress	Reference value	Equation (10)		ψ		
		x_ρ	ξ_ρ	180°	90°	0°
$\bar{\sigma}_{rrmax}$	1.525	1	m	1.538	1.528	1.538
			c	1.966	1.986	1.563
		0.5	m	1.548	1.538	1.548
			c	1.537	1.528	1.537
$\bar{\sigma}_{\theta\theta max}$	0.924	1	m	0.884	0.914	1.011
			c	0.988	0.973	0.944
		0.5	m	0.876	0.935	1.074
			c	0.885	0.912	1.004

Table 3. Stress values obtained at different ψ by varying ρ only according to Eq. (10).

Stress	Reference value	Equation (10)		ψ		
		$x_\rho = x_C$	ξ_{β^*}	180°	90°	0°
$\bar{\sigma}_{rrmax}$	1.525	1	m	1.541	1.531	1.544
			c	2.328	2.503	1.881
		0.5	m	1.629	1.563	1.575
$\bar{\sigma}_{\theta\theta max}$	0.924	1	m	0.877	0.890	1.079
			c	0.953	0.978	0.972
		0.5	m	0.886	0.856	1.845

Table 4. Stress values obtained at different ψ by varying ρ and C according to Eq. (10).

Afterwards, seeking further reductions in the stresses and/or raising the load-carrying capacity; C is added to ρ to follow Eq. (10). Table 4 illustrates the stresses values at different values of ψ and ξ_{β^*} .

Overall, results show that there would be a possibility to reduce the stresses by higher percentages compared to the case presented in Table 3. It can be emphasized that there is a fluctuation in the stresses' readings. However, at $\psi = 90^\circ$ with $\xi_{\beta^*} = m$, $\bar{\sigma}_{\theta\theta max}$ can be reduced by $\sim 7.3\%$ while $\bar{\sigma}_{rr max}$ witnesses an insignificant increase ($< 1\%$). This percentage of decline is greater by $\sim 2\%$ than the case where β^* only included ρ . Thus, including both ρ and C in Eq. (10) is more beneficial for the disc's behaviors if compared to changing ρ only, and the idea itself can produce encouraging outcomes (reducing failure/crack probability and raising the loading capacity). This showcases the originality of the proposed unconventional method.

On the other hand, it is not logical to investigate finite values of ψ and x_{β^*} , with different material properties, loads, and geometry. Therefore, it can be stated that performing an adequate optimization for the current problem's parameters is essential to produce the utmost stresses lessening levels, which is beyond the scope of the study.

Case (2): Magneto-thermoelastic (MTE) loading. In this case, more complications are seen compared to the previous problem. This is achieved by considering the existence of thermal loading which resembles a more practical scenario. For that sake, the following BCs are used: $T(r_i, \theta) = 100^\circ\text{C}$, and $T(r_o, \theta) = 500^\circ\text{C}$ with the previous ones listed in “Case (1): Magnetoelastic (ME) loading” Section. As seen in Fig. 6, $\bar{\sigma}_{rr max}$ stood at 2.6, $\bar{\sigma}_{\theta\theta min} = -4.289$, and $\bar{\sigma}_{r\theta} = \pm 0.27$. The last one would be neglected owing to its minor value²⁸. The concentration would be directed towards the first two ones even though the absolute value of $\bar{\sigma}_{\theta\theta min}$ is much larger than $\bar{\sigma}_{rr max}$. Nonetheless, it can be said that both are important for ceramics that have tensile strength far less than the corresponding compressive strength. Thus, it can be stated that even if results yielded moderate growth for $\bar{\sigma}_{\theta\theta max}$ and some dilatation for $\bar{\sigma}_{rr max}$, this can be pointed out to as a positive point.

Also, in this case, $\bar{\sigma}_{VM}$ (Fig. 6d) is included and discussed. It is calculated according to Eq. (20)⁸, and its dimensionless form is $\bar{\sigma}_{VM} = \sigma_{VM}/P_0$. Here, $\bar{\sigma}_{VM max}$ peaked at 3.87. It should be noted that $\bar{\sigma}_{VM max}$ is excluded from the previous case study since the objective is to prove the adequacy of the idea.

$$\sigma_{VM} = (\sigma_{rr}^2 - \sigma_{rr}\sigma_{\theta\theta} + \sigma_{\theta\theta}^2 + 3\sigma_{r\theta}^2)^{1/2} \quad (20)$$

Similar to the previous case, in order to apply the novel idea for stress reduction; Eq. (10) is used along with Eq. (9), where β^* would include: (1) ρ , (2) ρ and α , and (3) ρ , α and C. This is done in order to obtain the utmost applicable alleviations for the three stress values: $\bar{\sigma}_{rr max}$, $\bar{\sigma}_{\theta\theta min}$ and $\bar{\sigma}_{VM max}$.

Starting with ρ only in Eq. (10), a diverse variety of outcomes generated by altering ψ and x_ρ , and for brevity, selected cases are debated ($\psi = 180^\circ$ and 0°). At $\psi = 180^\circ$ with $x_\rho = 1$ and $\xi_\rho = c$, a tiny reduction of around 3% occurred for $\bar{\sigma}_{\theta\theta min}$ (Fig. 7b), whereas $\bar{\sigma}_{rr max}$ grew by about 17% according to Fig. 7a. Despite the fact that the increase is nearly six times the value of the decrease, $\bar{\sigma}_{VM max}$ is impacted moderately, as it declined by

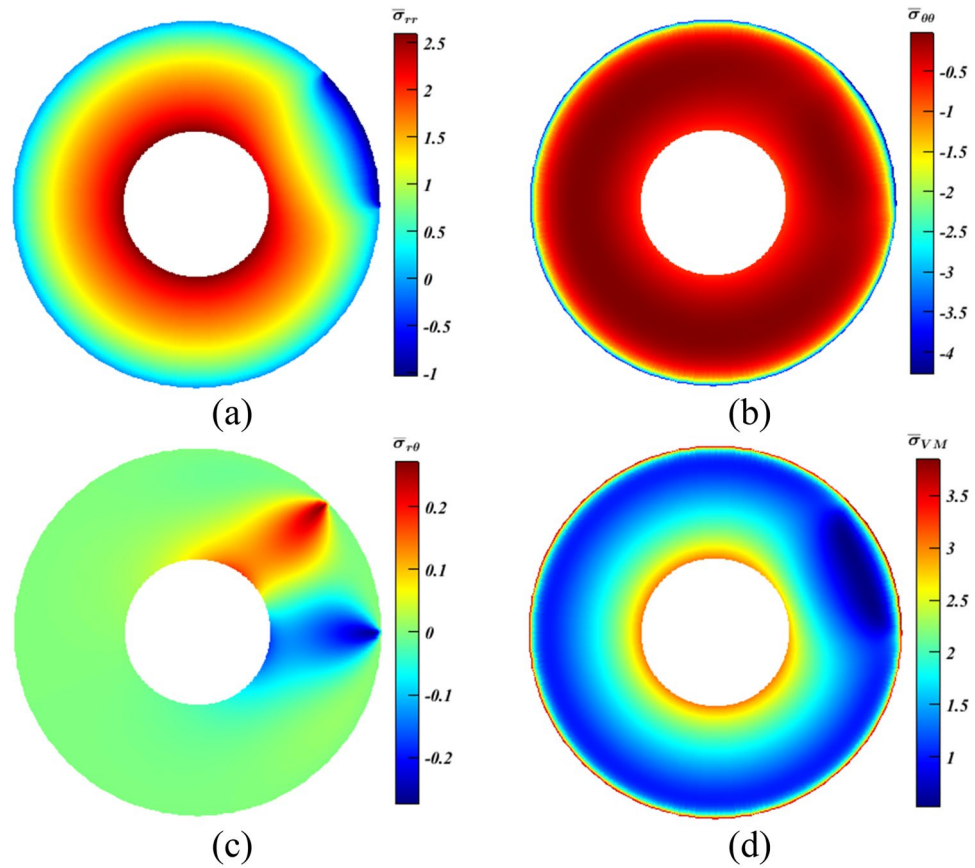


Figure 6. Dimensionless MTE stress contours for a rotating disc. (a) $\bar{\sigma}_{rr}$, (b) $\bar{\sigma}_{\theta\theta}$, (c) $\bar{\sigma}_{r\theta}$, and (d) $\bar{\sigma}_{VM}$.

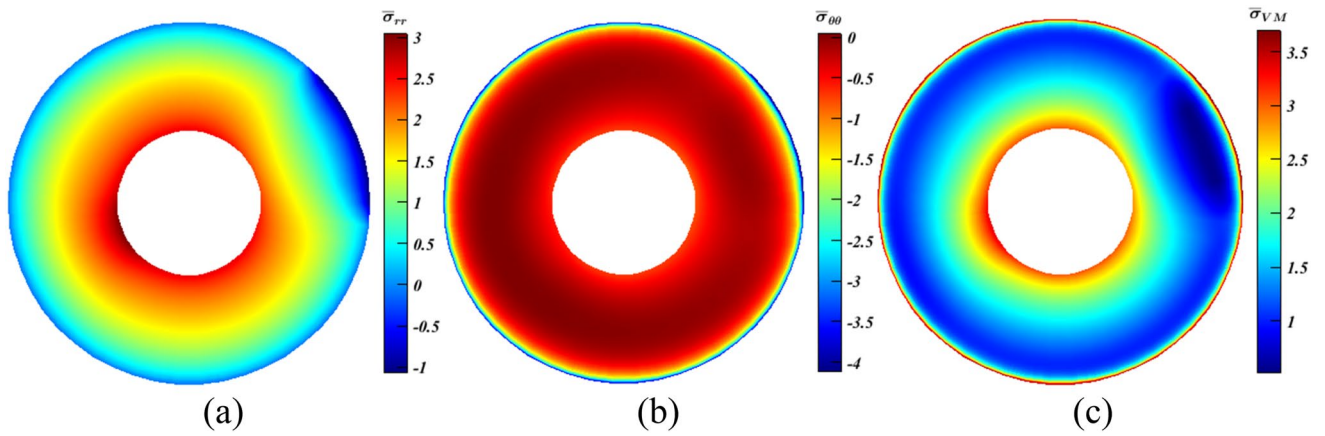


Figure 7. Dimensionless MTE stress contours for a rotating disc at $\psi = 180^\circ$ with $x_\rho = 1$ and $\xi_\rho = c$. (a) $\bar{\sigma}_{rr}$, (b) $\bar{\sigma}_{\theta\theta}$, and (c) $\bar{\sigma}_{VM}$.

nearly 3.5% as seen in Fig. 7c. This value experienced nearly a doubling hitting 6.2% at $\psi = 0^\circ$ with $x_\rho = 1$ and $\xi_\rho = c$ (Fig. 8c), where $\bar{\sigma}_{\theta\theta_{min}}$ (Fig. 8b) dropped by nearly 5.1% in contrast to $\bar{\sigma}_{rr_{max}}$ (Fig. 8a) that rose slightly by approximately 1.4%. On the contrary, results revealed that both $\bar{\sigma}_{rr_{max}}$ and $\bar{\sigma}_{\theta\theta_{min}}$ increased by < 1% and 8.5%, respectively, at similar ψ while $x_\rho = 0.5$ and $\xi_\rho = m$. Accordingly, $\bar{\sigma}_{VM_{max}}$ jumped by ~ 9%. Moreover, another interesting finding should be stated which is, while β^* only included ρ , results at $\xi_\rho = c$ are better than that at $\xi_\rho = m$. This is traced back to $\rho_c > \rho_m$; hence F_r becomes larger, and this works in opposite direction to the outer pressure especially at $\psi = 0^\circ$.

Based on these selected results, a maximum feasible decline of $\bar{\sigma}_{VM_{max}}$ is nearly 6.2% while β^* included ρ only. Thus, the novel proposed method within the manuscript could play an essential role in alleviating the stresses that can in turns lead to a reduction in the failure likelihood and an increase in the loading limits. Moreover,

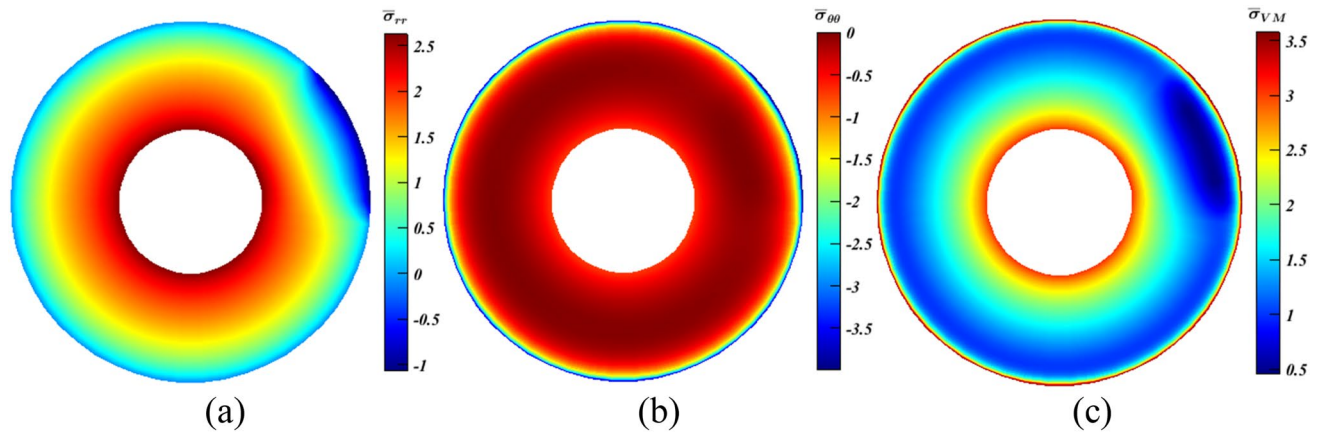


Figure 8. Dimensionless MTE stress contours for a rotating disc at $\psi = 0^\circ$ with $x_\rho = 1$ and $\xi_\rho = c$. (a) $\bar{\sigma}_{rr}$, (b) $\bar{\sigma}_{\theta\theta}$, and (c) $\bar{\sigma}_{VM}$.

Stress	Reference value	Equation (10)		ψ		
		$x_\rho = x_\alpha$	ξ_{β^*}	180°	90°	0°
$\bar{\sigma}_{rr_{max}}$	2.6	1	m	0.98	1.104	0.873
			c	22.9	26.770	10.4
		0.5	m	0.547	0.196	0.548
			c	-0.22	5.25	-0.2
$\bar{\sigma}_{\theta\theta_{min}}$	-4.289	1	m	114.2	116.453	128.5
			c	14.1	14.373	28.3
		0.5	m	42.3	42.506	56.6
			c	-0.97	5.9	14.83

Table 5. Stresses variations' percentages at different ψ by varying ρ and α based on Eq. (10).

seeking larger mitigation for the stresses; another trial is conducted through letting α join ρ in Eq. (10). Table 5 lists the variation percentage detected for both $\bar{\sigma}_{rr_{max}}$ and $\bar{\sigma}_{\theta\theta_{min}}$ according to the authors' records.

As seen, all the percentages are positive with different levels at $x_{\beta^*} = 1$. Conversely, at $x_{\beta^*} = 0.5$, $\bar{\sigma}_{rr_{max}}$ and $\bar{\sigma}_{\theta\theta_{min}}$ experienced some minor declines. Nevertheless, at the two values of x_{β^*} , $\bar{\sigma}_{VM_{max}}$ experienced gigantic surges that are traced back to the interaction between the loads, θ_p , material properties, and the geometry.

Another finding can be comprehended from Table 5 that is, at any ψ and $x_{\beta^*} = 0.5$, using $\xi_{\beta^*} = c$ yields smaller growths for $\bar{\sigma}_{\theta\theta_{min}}$ compared to using $\xi_{\beta^*} = m$. This concludes that using $\xi_\alpha = c$ would yield enhanced results compared to $\xi_\alpha = m$. In other words, the reduction of the prescribed area α is beneficial for the disc's performance as it reduces the thermal strains, and accordingly, the thermal stresses. However, generally, it can be drawn that under the current conditions, permitting β^* to include α along with ρ has deleterious consequences on the disc's performance.

Afterwards, as done in Case (1), Eq. (10) is extended to C as well as ρ and α so as to try achieving higher stress alleviation levels. Unfortunately, records disclose that both $\bar{\sigma}_{rr_{max}}$ and $\bar{\sigma}_{\theta\theta_{min}}$ increase substantially by using any value of ψ at $x_{\beta^*} = 1$. Hence, $\bar{\sigma}_{VM_{max}}$ goes up as well. For instance, at $\psi = 90^\circ$ with $x_{\beta^*} = 1$ and $\xi_{\beta^*} = c$ (Fig. 9), $\bar{\sigma}_{rr_{max}}$, $\bar{\sigma}_{\theta\theta_{min}}$ and $\bar{\sigma}_{VM_{max}}$ significantly soared by 87%, 23% and 36%, respectively.

In contrast, using $x_{\beta^*} = 0.5$ produced enhanced reductions for the three stresses as outlined in Table 6. It is seen that there are advantageous falls in the values of $\bar{\sigma}_{rr_{max}}$ and $\bar{\sigma}_{\theta\theta_{min}}$ leading to noteworthy plunges of $\bar{\sigma}_{VM}$ regardless of ψ . For example, at $\psi = 0^\circ$, $\bar{\sigma}_{VM_{max}}$ dropped by approximately 8.9% and 9.9% at $\xi_{\beta^*} = m$ and c , respectively, and these two values surpass the applicable reductions levels at $\psi = 90^\circ$ and 180° . These results again prove that there would be stresses' reductions and an increase for the loading capacity through using the method proposed within this study.

Finally, and opposing to the previous results where x_{β^*} has an equal value for the three properties; having different configurations of it are examined at only $\psi = 0^\circ$. For that sake, the following values were used: $\xi_\rho = \xi_\alpha = c$, $\xi_C = m$, $x_\rho = 1$, $x_\alpha = 0.25$, and $x_C = 1, 0.5$ or 0.25 .

As portrayed in Fig. 10a, $\bar{\sigma}_{rr_{max}}$ witnessed substantial increase ($\sim 8\%$), while in Figs. 11a and 12a, it experienced slight declines ($< 2\%$). Conversely, $\bar{\sigma}_{\theta\theta_{min}}$ fell by approximately 19.8% at $x_C = 1$ (Fig. 10b), and continued to decrease reaching more or less than 20.7%, which can be considered as a great achievement, at $x_C = 0.5$ and 0.25 as seen in Figs. 11b and 12b, respectively. Thus, according to the readings of $\bar{\sigma}_{rr_{max}}$ and $\bar{\sigma}_{\theta\theta_{min}}$, the smaller the value of x_C , the higher the stresses' reductions are attainable. However, this is not dominant for the values

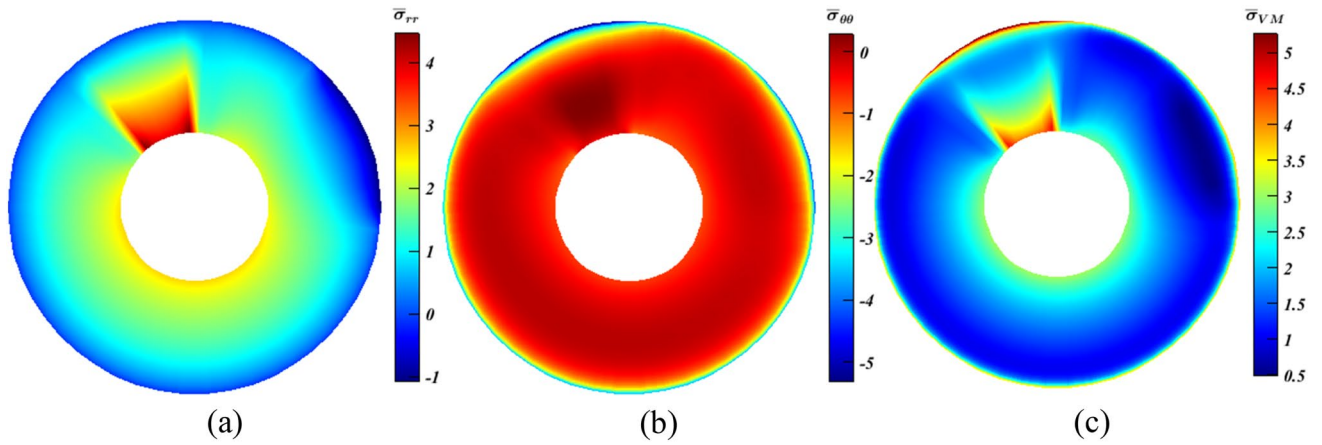


Figure 9. Dimensionless MTE stress contours for a rotating disc at $\psi = 90^\circ$ with $x_{\beta^*} = 1$ and $\xi_{\beta^*} = c$. (a) $\bar{\sigma}_{rr}$, (b) $\bar{\sigma}_{\theta\theta}$, and (c) $\bar{\sigma}_{VM}$. β^* includes C , ρ and α .

Stress	Reference value	ξ_{β^*}	ψ		
			180°	90°	0°
$\bar{\sigma}_{rr_{max}}$	2.6.	m	-0.457	-0.367	-0.158
		c	-0.392	1.976	-0.340
$\bar{\sigma}_{\theta\theta_{min}}$	-4.289	m	-1.352	-2.578	-17.2
		c	-1.923	-3.630	-18.109
$\bar{\sigma}_{VM_{max}}$	3.87	m	-1.456	-2.775	-8.97
		c	-2.070	-3.906	-9.9

Table 6. Stress variation percentage at different ψ by varying ρ , α and C according to Eq. (10) using $x_{\beta^*} = 0.5$.

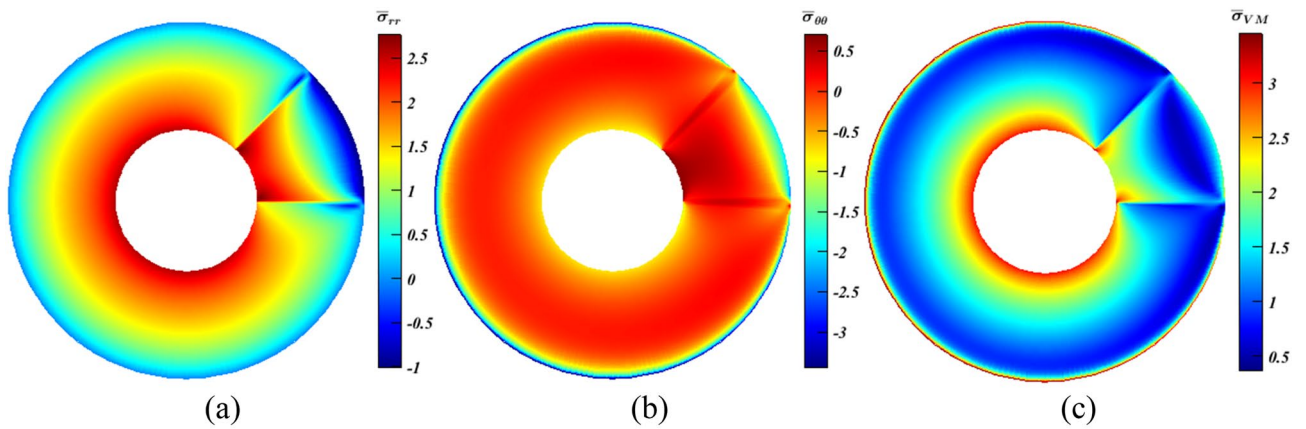


Figure 10. Dimensionless MTE stress contours for a rotating disc at $\psi = 0^\circ$ with $x_\rho = x_C = 4x_\alpha = 1$, $\xi_\rho = \xi_\alpha = c$ and $\xi_C = m$. (a) $\bar{\sigma}_{rr}$, (b) $\bar{\sigma}_{\theta\theta}$, and (c) $\bar{\sigma}_{VM}$.

of $\bar{\sigma}_{VM_{max}}$. At $x_C = 1$ (Fig. 10c), it dropped by a large value ($\sim 10.8\%$), and continued to declined hitting nearly 12.5% at $x_C = 0.5$ (Fig. 11c). As x_C shrinks to 0.25, a lessening of 10.5% is experienced as seen in Fig. 12c.

These results prove the valuable impacts of the idea of keeping some the properties constant through a selected area within the disc to reduce the failure likelihood and/or raise the working load capacity and safety. They also confirm that the problem in hand is nonlinear; thus, the behaviors are hardly predicted. Accordingly, performing an adequate optimization is central to obtain the most suitable values of x_{β^*} and ψ . Additionally, it opens new horizons through considering more properties within the prescribed area that can have different values of ψ other the one used within the current study.

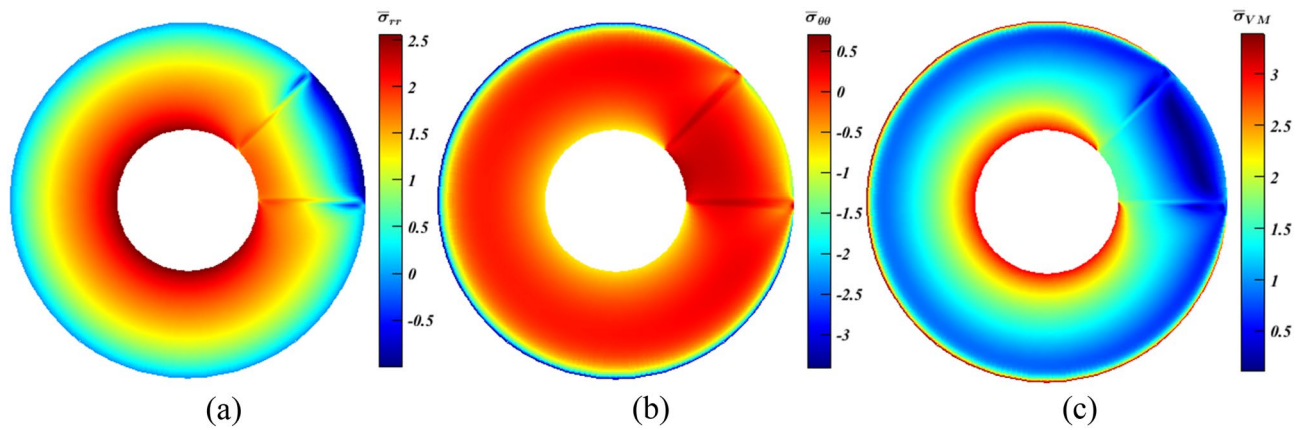


Figure 11. Dimensionless MTE stress contours for a rotating disc at $\psi = 0^\circ$ with $x_\rho = 2x_C = 4x_\alpha = 1$, $\xi_\rho = \xi_\alpha = c$ and $\xi_C = m$. (a) $\bar{\sigma}_{rr}$, (b) $\bar{\sigma}_{\theta\theta}$, and (c) $\bar{\sigma}_{VM}$.

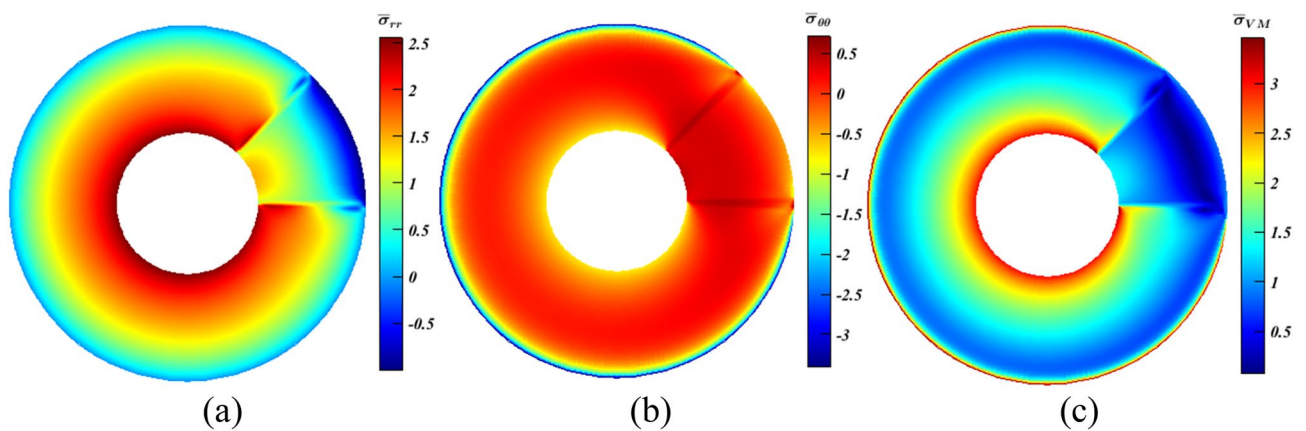


Figure 12. Dimensionless MTE stress contours for a rotating disc at $\psi = 0^\circ$ with $x_\rho = 4x_C = 4x_\alpha = 1$, $\xi_\rho = \xi_\alpha = c$ and $\xi_C = m$. (a) $\bar{\sigma}_{rr}$, (b) $\bar{\sigma}_{\theta\theta}$, and (c) $\bar{\sigma}_{VM}$.

Conclusion

The main contribution of this article is trying to open new horizons for lowering the magnetoelastic/magneto-thermoelastic stresses and/or increasing the working limits of rotating FGM discs. This was sought through an atypical idea that presumes the existence of an area within the disc with definite dimensions, location, and particular homogeneous properties. The assumption of perfect bonding between this area and the FGM area was utilized in the analyses. The solution of the governing equations was performed through FEM.

Overall, results showed that some constructive stress reductions were achievable depending on the location and the chosen constant properties of the prescribed area. A decline of $\sim 7.3\%$ in the maximum tensile tangential stress occurred for the ME loading case. This percentage jumped to nearly 20.7% at the MTE case, which led to mitigation of the von Mises stress by about 12.5% at certain composition for the homogenous area.

These results were indisputably beneficial for decreasing the crack formation/propagation likelihood and/or raising the payload limits, which proves the originality of the proposed method. However, optimizing many parameters is recommended to obtain the utmost stresses suppression especially for such nonlinear problems. These parameters include, for instance, thickness, property and its fraction, location, and the dimension of the homogenous area.

Data availability

The datasets generated and/or analyzed during the current study are not publicly available due to being part of an ongoing study but are available from the first or the third authors on a reasonable request.

Received: 14 June 2023; Accepted: 1 August 2023

Published online: 21 August 2023

References

1. Trinh, M.-C. & Kim, S.-E. Nonlinear thermomechanical behaviors of thin functionally graded sandwich shells with double curvature. *Compos. Struct.* **195**, 335–348. <https://doi.org/10.1016/j.compstruct.2018.04.067> (2018).

2. Trinh, M.-C. & Kim, S.-E. Nonlinear stability of moderately thick functionally graded sandwich shells with double curvature in thermal environment. *Aerosp. Sci. Technol.* **84**, 672–685. <https://doi.org/10.1016/j.ast.2018.09.018> (2019).
3. Hojjati, M. H. & Jafari, S. Semi-exact solution of elastic non-uniform thickness and density rotating disks by homotopy perturbation and Adomian's decomposition methods. Part I: Elastic solution. *Int. J. Press. Vessels Pip.* **85**(12), 871–878. <https://doi.org/10.1016/j.ijpvp.2008.06.001> (2008).
4. Hosseini, M., Shishesaz, M. & Hadi, A. Thermoelastic analysis of rotating functionally graded micro/nanodisks of variable thickness. *Thin-Walled Struct.* **134**, 508–523. <https://doi.org/10.1016/j.tws.2018.10.030> (2019).
5. Elhefny, A. & Liang, G. Stress and deformation of rocket gas turbine disc under different loads using finite element modelling. *Propuls. Power Res.* **2**(1), 38–49. <https://doi.org/10.1016/j.jprr.2013.01.002> (2013).
6. Sharma, D., Kaur, R. & Sharma, H. Investigation of thermo-elastic characteristics in functionally graded rotating disk using finite element method. *Nonlinear Eng.* **10**(1), 312–322. <https://doi.org/10.1515/nleng-2021-0025> (2021).
7. Nayak, P., Bhowmick, S. & Saha, K. N. Elasto-plastic analysis of thermo-mechanically loaded functionally graded disks by an iterative variational method. *Eng. Sci. Technol. Int. J.* **23**(1), 42–64. <https://doi.org/10.1016/j.jestch.2019.04.007> (2020).
8. Eldeeb, A. M., Shabana, Y. M. & Elsawaf, A. Influences of angular deceleration on the thermoelastoplastic behaviors of nonuniform thickness multilayer FGM discs. *Compos. Struct.* **258**, 113092. <https://doi.org/10.1016/j.compstruct.2020.113092> (2020).
9. Eldeeb, A. M., Shabana, Y. M. & Elsawaf, A. Thermo-elastoplastic behavior of a rotating sandwich disc made of temperature-dependent functionally graded materials. *J. Sandw. Struct. Mater.* **23**(5), 1761–1783. <https://doi.org/10.1177/1099636220904970> (2021).
10. Jodaeei, A., Jalal, M. & Yas, M. H. Free vibration analysis of functionally graded annular plates by state-space based differential quadrature method and comparative modeling by ANN. *Compos. B Eng.* **43**(2), 340–353. <https://doi.org/10.1016/j.compositesb.2011.08.052> (2012).
11. Al-Furjan, M. S. H. *et al.* On the dynamics of the ultra-fast rotating cantilever orthotropic piezoelectric nanodisk based on nonlocal strain gradient theory. *Compos. Struct.* **255**, 112990. <https://doi.org/10.1016/j.compstruct.2020.112990> (2021).
12. Sarkar, P. R. & Rahman, A. S. Effect of magnetic field on the thermo-elastic response of a rotating FGM circular disk with non-uniform thickness. *J. Strain Anal. Eng. Des.* **57**(2), 116–131. <https://doi.org/10.1177/03093247211005215> (2022).
13. Yousefabad, E. K. *et al.* The effect of non-uniform combustion temperature profile on thermal fatigue cracking of an air-cooled gas turbine vane. *Eng. Fail. Anal.* **105**, 766–780. <https://doi.org/10.1016/j.engfailanal.2019.07.008> (2019).
14. Akbari, M. R. & Ghanbari, J. Analytical exact solution for functionally graded rotating disks under non-symmetric thermal and mechanical loads. *Mater. Res. Express* **6**(5), 056545. <https://doi.org/10.1088/2053-1591/ab06d7> (2019).
15. Bayat, M. *et al.* One-dimensional analysis for magneto-thermo-mechanical response in a functionally graded annular variable-thickness rotating disk. *Appl. Math. Model.* **38**(19–20), 4625–4639. <https://doi.org/10.1016/j.apm.2014.03.008> (2014).
16. Zenkour, A. M. & Abbas, I. A. Magneto-thermoelastic response of an infinite functionally graded cylinder using the finite element method. *J. Vib. Control* **20**(12), 1907–1919. <https://doi.org/10.1177/1077546313480541> (2014).
17. Abbas, I. A. & Zenkour, A. M. LS model on electro-magneto-thermoelastic response of an infinite functionally graded cylinder. *Compos. Struct.* **96**, 89–96. <https://doi.org/10.1016/j.compstruct.2012.08.046> (2013).
18. Dini, A., Nematollahi, M. A. & Hosseini, M. Analytical solution for magneto-thermo-elastic responses of an annular functionally graded sandwich disk by considering internal heat generation and convective boundary condition. *J. Sandw. Struct. Mater.* **23**(2), 542–567. <https://doi.org/10.1177/1099636219839161> (2019).
19. Behravan Rad, A. & Shariyat, M. Three-dimensional magneto-elastic analysis of asymmetric variable thickness porous FGM circular plates with non-uniform tractions and Kerr elastic foundations. *Compos. Struct.* **125**, 558–574. <https://doi.org/10.1016/j.compstruct.2015.02.049> (2015).
20. Dai, H. L., Fu, Y. M. & Dong, Z. M. Exact solutions for functionally graded pressure vessels in a uniform magnetic field. *Int. J. Solids Struct.* **43**(18), 5570–5580. <https://doi.org/10.1016/j.ijsolstr.2005.08.019> (2006).
21. Akbari, M. R. & Ghanbari, J. Discussion on “exact solutions for functionally graded pressure vessels in a uniform magnetic field”. *Int. J. Solids Struct.* **78–79**, 216–218. <https://doi.org/10.1016/j.ijsolstr.2015.09.003> (2016).
22. Zenkour, A. M. On the magneto-thermo-elastic responses of FG annular sandwich disks. *Int. J. Eng. Sci.* **75**, 54–66. <https://doi.org/10.1016/j.ijengsci.2013.11.001> (2014).
23. Shabana, Y. M. *et al.* Stresses minimization in functionally graded cylinders using particle swarm optimization technique. *Int. J. Press. Vessels Pip.* **154**, 1–10. <https://doi.org/10.1016/j.ijpvp.2017.05.013> (2017).
24. Eldeeb, A. M., Shabana, Y. M. & Elsawaf, A. Particle swarm optimization for the thermoelastic behaviors of functionally graded rotating nonuniform thickness sandwich discs. *Arab. J. Sci. Eng.* **48**, 4067–4079. <https://doi.org/10.1007/s13369-022-07351-x> (2023).
25. Eldeeb, A., Shabana, Y. & Elsawaf, A. Thermoelastic stress mitigation and weight reduction of functionally graded multilayer nonuniform thickness disc. *J. Strain Anal. Eng. Des.* <https://doi.org/10.1177/03093247231165091> (2023).
26. Nemat-Alla, M., Ahmed, K. I. E. & Hassab-Allah, I. Elastic-plastic analysis of two-dimensional functionally graded materials under thermal loading. *Int. J. Solids Struct.* **46**(14), 2774–2786. <https://doi.org/10.1016/j.ijsolstr.2009.03.008> (2009).
27. Miao, X.-Y. *et al.* Free vibration analysis of three-layer thin cylindrical shell with variable thickness two-dimensional FGM middle layer under arbitrary boundary conditions. *J. Sandwich Struct. Mater.* **24**(2), 973–1003. <https://doi.org/10.1177/10996362211020429> (2021).
28. Eldeeb, A. M. *et al.* Thermoelastic stresses alleviation for two-dimensional functionally graded cylinders under asymmetric loading. *J. Therm. Stresses* **46**(1), 59–74. <https://doi.org/10.1080/01495739.2022.2151960> (2023).
29. Zhou, S. & Li, Q. Microstructural design of connective base cells for functionally graded materials. *Mater. Lett.* **62**(24), 4022–4024. <https://doi.org/10.1016/j.matlet.2008.05.058> (2008).
30. Su, Y. *et al.* Influence of composition gradient variation on the microstructure and mechanical properties of 316 L/Inconel718 functionally graded material fabricated by laser additive manufacturing. *J. Mater. Process. Technol.* **283**, 116702. <https://doi.org/10.1016/j.jmatprotec.2020.116702> (2020).
31. Oziablo, A. *et al.* Microstructure of Al₂O₃-Fe FGM obtained by modified slip-casting method. *Mater. Sci. Forum* **492–493**, 665–672. <https://doi.org/10.4028/www.scientific.net/MSF.492-493.665> (2005).
32. Su, Z., *et al.* Characterization of Mechanical Property of PLA-ABS Functionally Graded Material Fabricated by Fused Deposition Modeling. In *ASME 2021 Gas Turbine India Conference*. (2021).
33. Saadatfar, M. & Zarandi, M. H. Effect of angular acceleration on the mechanical behavior of an exponentially graded piezoelectric rotating annular plate with variable thickness. *Mech. Based Des. Struct. Mach.* <https://doi.org/10.1080/15397734.2020.1751198> (2020).
34. Vullo, V. & Vivio, F. *Rotors: Stress Analysis and Design* (Springer, 2013).
35. Eldeeb, A. M., Shabana, Y. M. & Elsawaf, A. Investigation of the thermoelastoplastic behaviors of multilayer FGM cylinders. *Compos. Struct.* **276**, 114523. <https://doi.org/10.1016/j.compstruct.2021.114523> (2021).
36. Chawde, D. P. & Bhandakkar, T. K. Mixed boundary value problems in power-law functionally graded circular annulus. *Int. J. Press. Vessels Pip.* **192**, 104402. <https://doi.org/10.1016/j.ijpvp.2021.104402> (2021).
37. Saadatfar, M., Zarandi, M. & Babelahi, M. Effects of porosity, profile of thickness, and angular acceleration on the magneto-electro-elastic behavior of a porous FGME rotating disc placed in a constant magnetic field. *Proc. Inst. Mech. Eng. C J. Mech. Eng. Sci.* **235**(7), 1241–1257. <https://doi.org/10.1177/0954406220938409> (2021).

38. Li, H. & Liu, Y. Functionally graded hollow cylinders with arbitrary varying material properties under nonaxisymmetric loads. *Mech. Res. Commun.* **55**, 1–9. <https://doi.org/10.1016/j.mechrescom.2013.10.011> (2014).
39. Reddy, J. N. & Gartling, D. K. *The Finite Element Method in Heat Transfer and Fluid Dynamics* (CRC Press, 2010).
40. Machado, G. G. *et al.* Numerical simulation by the finite element method of the constructive steps of a precast prestressed segmental bridge. *Struct. Eng. Mech.* **85**(2), 163–177. <https://doi.org/10.12989/sem.2023.85.2.163> (2023).
41. Ferreira, A. J. M. & Fantuzzi, N. Plane Stress. In *MATLAB Codes for Finite Element Analysis: Solids and Structures* 171–205 (Springer, 2020).
42. Logan, D. L. *A first course in the finite element method* (Cengage Learning, 2016).
43. Hassani, A. *et al.* Semi-exact elastic solutions for thermo-mechanical analysis of functionally graded rotating disks. *Compos. Struct.* **93**(12), 3239–3251. <https://doi.org/10.1016/j.compstruct.2011.06.001> (2011).
44. Noda, N. *Thermal stresses* (CRC Press, 2002).

Author contributions

A. M. Eldeeb wrote the main manuscript text, while Y. M. Shabana and A. Elsawaf provided supervision throughout all stages of the paper. T. A. El-Sayed reviewed the paper. All authors participated in the manuscript review process.

Funding

Open access funding provided by The Science, Technology & Innovation Funding Authority (STDF) in cooperation with The Egyptian Knowledge Bank (EKB). This research did not receive any specific grant from funding agencies in the public, commercial, or not-for-profit sectors.

Competing interests

The authors declare no competing interests.

Additional information

Correspondence and requests for materials should be addressed to T.A.E.-S.

Reprints and permissions information is available at www.nature.com/reprints.

Publisher's note Springer Nature remains neutral with regard to jurisdictional claims in published maps and institutional affiliations.



Open Access This article is licensed under a Creative Commons Attribution 4.0 International License, which permits use, sharing, adaptation, distribution and reproduction in any medium or format, as long as you give appropriate credit to the original author(s) and the source, provide a link to the Creative Commons licence, and indicate if changes were made. The images or other third party material in this article are included in the article's Creative Commons licence, unless indicated otherwise in a credit line to the material. If material is not included in the article's Creative Commons licence and your intended use is not permitted by statutory regulation or exceeds the permitted use, you will need to obtain permission directly from the copyright holder. To view a copy of this licence, visit <http://creativecommons.org/licenses/by/4.0/>.

© The Author(s) 2023